

On the Heterogeneity of Local Shear Strain Induced by High-Pressure Torsion

Wei Jiang, Hao Zhou, Yang Cao,* Jinfeng Nie, Yusheng Li, Yonghao Zhao, Megumi Kawasaki, Terence G. Langdon, and Yuntian Zhu*

A ductile duplex stainless steel consisting of a ferrite phase and an austenitic phase is chosen as a model material to investigate the development of shear strain patterns under high-pressure torsion. Systematic analysis on the macroscopic and microscopic heterogeneities of local shear strain reveals that complex shear patterns can be developed only above a high strain level where the grain sizes are already refined to a steady state. It is concluded that grain boundary-mediated deformation mechanisms provide sufficient freedom for reshaping the austenite phase domains, and thus the intrinsic factor required for the formation of these complicated shear patterns is well-developed ultrafine grains and/or nanograins.

1. Introduction

High-pressure torsion (HPT) is so far the most effective severe plastic deformation (SPD) method for processing bulk nanostructured materials.^[1] After 30 years of research and development in this field, researchers have achieved substantial understanding about this method and the corresponding effects on the microstructures and mechanical properties of materials.^[2–4]

The principle of quasi-constrained HPT is illustrated schematically in **Figure 1a**. A disk-shaped sample is placed between two massive anvils and subjected to an applied pressure P in the range between a few hundred MPa to a few tens of GPa.


Dr. W. Jiang, Dr. H. Zhou, Dr. Y. Cao, Dr. J. Nie, Dr. Y. Li, Prof. Y. Zhao, Prof. Y. Zhu

Nano and Heterogeneous Materials Center
School of Materials Science and Engineering
Nanjing University of Science and Technology
Nanjing 210094, P. R. China
E-mail: y.cao@njust.edu.cn; ytzhu@ncsu.edu

Prof. M. Kawasaki
School of Mechanical, Industrial and Manufacturing Engineering
Oregon State University
Corvallis, OR 97331-6001, USA

Prof. T. G. Langdon
Materials Research Group
Department of Mechanical Engineering
University of Southampton
Southampton SO17 1BJ, UK

Prof. Y. Zhu
Department of Materials Science and Engineering
North Carolina State University
Raleigh, NC 27695, USA

 The ORCID identification number(s) for the author(s) of this article can be found under <https://doi.org/10.1002/adem.201900477>.

DOI: 10.1002/adem.201900477

Then torsional strain is imposed by the rotation of either the lower or the upper anvil. The compressive load/pressure imposed on the disk, which is constrained in the cavity between the upper and lower anvils, is effective in preventing cracking of the sample. The torsion provided by the rotating anvil is theoretically capable of imposing unlimited strain to the sample. Figure 1b shows the 3D reconstruction of a half HPT disk, which is a simple 3D drawing based on the optical images taken from the exposed surfaces of a half ten-revolutions HPT disk. The HPT disk would

eventually deform to a shape that fits well in the cavity between the anvils. The rough surface of the cavity provides excellent grip to the disk but leaves marks on the disk surface. The high strain imposed by HPT causes noteworthy microstructural evolution to the sample material and this is revealed on the polished cross sections of the disk.

There are also unconstrained and constrained HPT setups and these are described in more detail in previous studies.^[1,5,6] Despite the different HPT setups, the basic principle of HPT is the same so that the equivalent von Mises strain imposed on the HPT disk is given by a relationship

$$\varepsilon_{\text{eq}} = \frac{2\pi Nr}{h\sqrt{3}} \quad (1)$$

where N is the number of HPT revolutions, r is the radial distance from the center of the disk, and h is the disk thickness. Equation (1) indicates that there will always be a strain gradient with a low strain at the disk center and high strain at the disk periphery. Equation (1) also indicates that the shear strain at the same radial distance to the center will be the same. However, there have been numerous reports showing that the actual shear strain imposed by HPT may deviate significantly from the ideal situation described by Equation (1)^[7–10] and these results demonstrate hardly predictable heterogeneity throughout the disk sample. The early discovery of the heterogeneity of local shear strain induced by HPT was by means of mapping the hardness throughout the surface of an HPT disk,^[7,11] but the indirect measurement of shear strain was not able to fully explain the phenomenon. Nature abounds with visible patterns of various kinds as does shear strain. In 2010, Cao et al.^[10,12,13] proposed a method of visualizing shear strain using ductile dual-phase materials with easily distinguishable phase domain structures. Since then, the study on shear strain imposed by HPT became much easier,^[5,14–16] and it was quickly realized that the

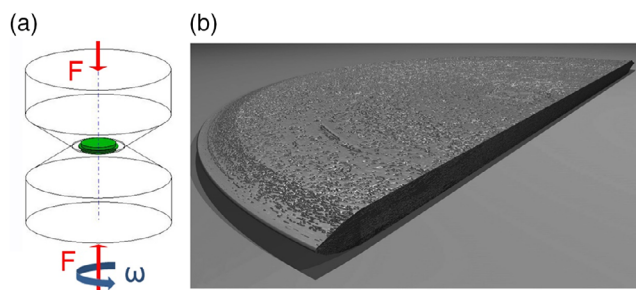


Figure 1. a) A schematic illustration of the HPT process. b) A 3D reconstruction of a half HPT disk where the morphology of the top surface and the microstructure on the cross-sectional face are revealed.

heterogeneity of local shear strain was a result of local shear turbulence, shear vortices, and shear bands.^[10,13,14]

Macroscopic shear strain heterogeneity can be well explained by the existence of bifurcations under plastic flow, including shear turbulence, shear vortices, and shear bands. However, there is also microscopic shear strain heterogeneity, which is inherent to the characteristics of crystal structures and slip systems. For example, an allotropic phase transformation during deformation may cause heterogeneity in local shear strain^[17,18] and the asymmetric natures of twinning and slip in polycrystalline face-centered cubic (FCC) and hexagonal close-packed (HCP) materials may cause heterogeneities in local shear strain.^[4,19] In contrast to the macroscopic shear strain heterogeneity, which is revealed as flow patterns of irregular shapes, the microscopic shear strain heterogeneity is revealed as phase boundaries and domain boundaries of irregular shapes. The nanostructured materials processed by SPD are often referred to as interface-controlled materials because the spatial arrangements of grain boundaries, phase boundaries, and domain boundaries predominantly govern the mechanical properties of these materials.^[3,20,21] Thus, the microscopic heterogeneity of local shear strain imposed by HPT is obviously another fundamental issue in mastering the HPT process.

Despite the fact that the macroscopic shear strain heterogeneity and the microscopic shear strain heterogeneity are equally important in the basic principles of the HPT processing of metallic materials, there is no research investigating the correlation between the heterogeneities of different scales. Thus, the current study examines both the macroscopic shear strain heterogeneity and the microscopic shear strain heterogeneity introduced by the HPT processing of duplex stainless steels. The relationship between the heterogeneities of different scales is explained in detail based on the macrostructural and microstructural evolution of the materials with increasing strain.

2. Results

The commercial DP3W duplex stainless steel has equal volume fractions of α -phase and γ -phase. Both phases are ductile and easily recognizable under an optical microscope (OM) and scanning electron microscope (SEM), thereby making the material ideal for visualization of shear strain. As shown in **Figure 2**, the α -phase matrix appears in dark contrast and the γ -phase domains appear

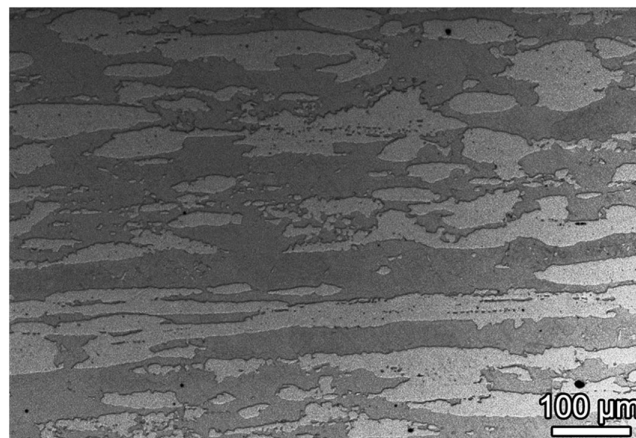


Figure 2. An optical micrograph showing lamellar austenite phase domains embedded in the dark contrast ferrite matrix.

in light contrast under an OM. A 3D reconstruction of the structure shows that the γ -phase domains have lengths of 100–1000 μm and an elliptical cross section with long widths of 10–100 μm and short widths of 5–50 μm . By increasing HPT strain, the shapes and orientations of the γ -phase domains are gradually changed. As shown in **Figure 3a**, when the disk was processed to three revolutions under 6 GPa pressure, the majority of the γ -phase domains tend to reorient toward the direction of the HPT rotation. However, in general, the shear strain pattern appears chaotic and inhomogeneous. When the disk was processed to 16 revolutions, the shear strain pattern was very close to the ideal situation in which the majority of the phase domains are parallel to the direction of the HPT-imposed strain (parallel to the circumference of the disk). However, in this particular case, shear turbulence and shear vortices are still abundant in the regions approximately 1 mm from the disk circumference. This is due to the gradient back-pressure experienced at the circumference of the disk and the anvil misalignment.^[14]

There are numerous results showing that macroscopic heterogeneity is evident prior to reaching homogeneous microstructures. In the case of high-strength materials such as steels, macroscopic heterogeneity is abundant when samples are processed to 3–5 revolutions.^[12–14] The major features of local shear heterogeneities are sharp shear bands, as marked by red arrows in **Figure 4**, shear turbulence shown in **Figure 4c**, and shear vortices shown in **Figure 4d**, where **Figure 4a,b** was taken at the edge of the disk and **Figure 4c,d** was taken approximately 1.5 mm away from the edge of the disk. Shear bands are mostly observed at the edge of the disks, but shear turbulence and shear vortices may exist at any location on the disk surface except the disk center. Shear bands are very effective in causing distortion to local shear strain patterns and fragmentation to the local microstructures,^[22,23] indicated by the sharp changes in shear patterns on both sides of the shear bands as shown in **Figure 4**.

The heterogeneity induced by HPT processing is also examined at the microscale. At this level, local shear strain is reflected by the shape of the grains and phase domains and by the trace of grain boundaries and phase boundaries. For comparison, the microstructures of the as-received steel samples were examined

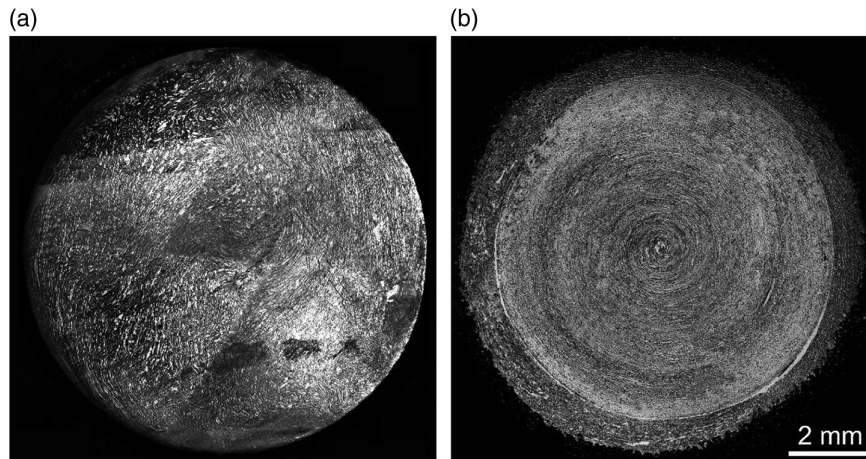


Figure 3. Optical micrographs showing top surfaces of HPT disks processed a) to three revolutions under 6 GPa pressure and b) to 16 revolutions under 8 GPa pressure, respectively.

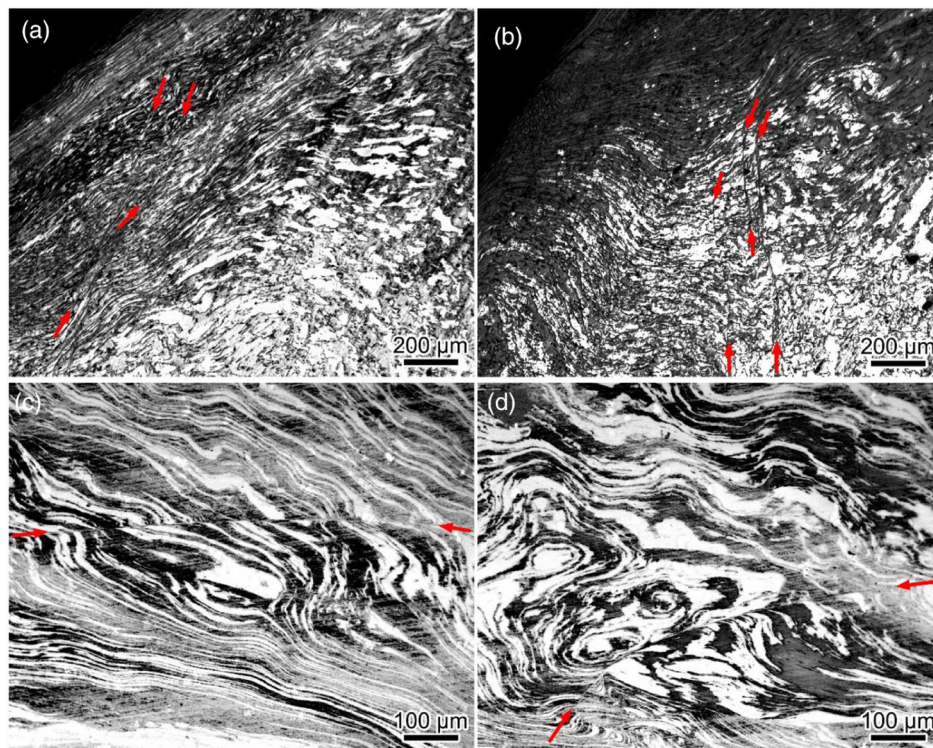


Figure 4. Optical micrographs showing macroscopic shear strain patterns in HPT disks: a,b) are taken from the top surface of the disk processed to three revolutions under 6 GPa pressure; c,d) are taken from the top surface of the disk processed to five revolutions under 6 GPa pressure. Red arrows mark sharp shear bands.

first. As shown in **Figure 5**, the α -phase and the γ -phase appear in light and dark contrast, respectively, because the γ -phase in the steel contains a large proportion of Ni atoms which are much more effective in scattering electrons than Fe atoms. Diffraction patterns in **Figure 5b,c** are taken from the grains labeled α and γ , respectively, to justify the crystal structures of the α -phase and the γ -phase. The grain boundaries and phase boundaries in the as-received samples are smooth and sharp. Dislocation

densities in both phases are low, indicating very low strain and low residual stresses in both phases.

As shown in **Figure 6**, where the theoretical von Mises strain is in the range of 2–5 (near the center of 1-revolution HPT disk), the austenite grain is featured with a high density of nano-twins, and the α -phase region is featured with ultrafine subgrains. In this case, the interface between the α -phase and the γ -phase is also the grain boundary of the austenite grain. The austenite grain

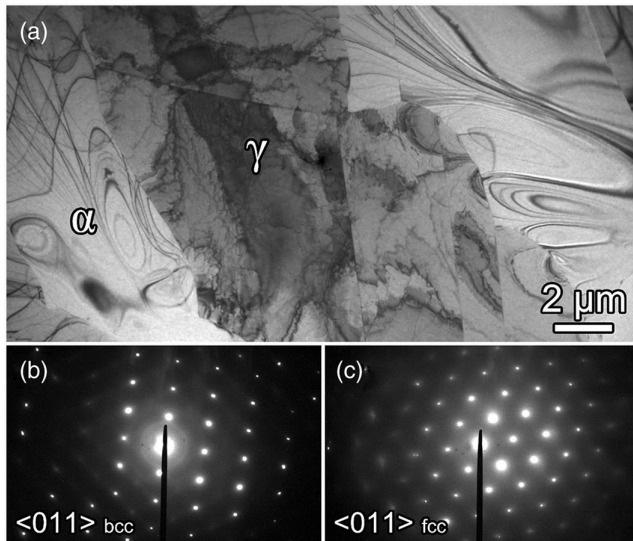


Figure 5. a) A TEM image showing microstructures of α -phase and γ -phase in an as-received DP3W duplex stainless steel sample. b,c) are diffraction patterns for the α -phase-grain and γ -phase-grain labeled in (a), respectively.

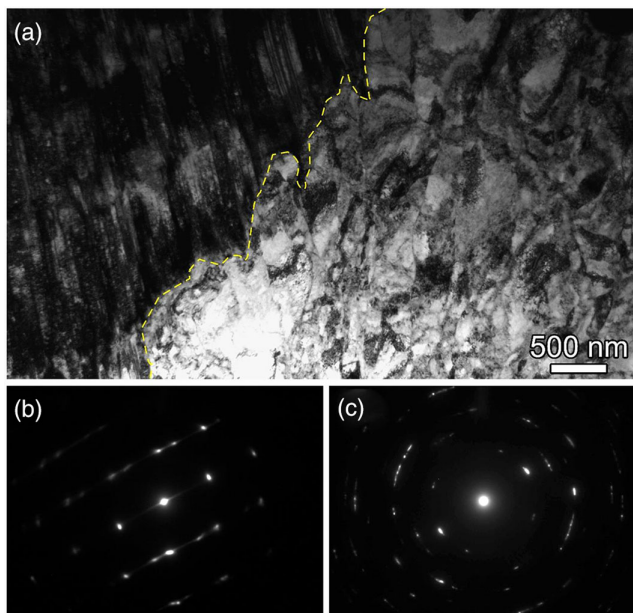


Figure 6. a) A TEM image showing microstructures of α -phase and γ -phase near the center of a HPT disk processed to one revolution under 6 GPa pressure. b,c) are diffraction patterns for the γ -phase and α -phase, respectively.

boundary is no longer smooth in contrast to the grain boundaries in the as-received sample (Figure 5). Numerous twin boundaries attached to the grain boundary indicate that deformation twinning is a major contributor to the shear strain experienced by the austenite grain.^[24–26] It is worth noting that dislocation slip also plays an important role in accommodating the shear strain in the austenite grain, but the freedom of dislocation motion is

strongly restricted by the twin boundaries.^[27] In contrast, 3D dislocation structures were formed in accommodating the shear strain in the α -phase matrix, granting the α -phase matrix the freedom of changing to any complex shape.

As the equivalent von Mises strain increased to the range of 5–20, the γ -phase close to the center of the steel disk possesses a mixture of ultrafine subgrains and fragmented twin bundles, as shown in Figure 7. The grain containing a high density of nanotwins was sliced into a few parallel pieces by the white bands. The angle between the white bands and the $\{111\}$ twinning plane is approximately 70° . An early report has shown that parallel primary twins could lose coherency and become thin-band structures with an angle of 60° – 70° to a $\{111\}$ twinning plane under increased shear strain.^[28,29] In contrast, the angle between the $\{111\}$ twinning planes and a microscopic shear band is usually much smaller in the range of 20° – 40° .^[29,30] Therefore, the white bands were primary twins which lost coherency after interaction with secondary twins and dislocations. It is worth mentioning that microscopic shear bands have been observed in some materials with low stacking-fault energies processed by HPT.^[31] However, microscopic shear bands were not observed in HPT-processed duplex stainless steels, despite the low stacking-fault energy of the γ -phase.^[28] There are a few possible reasons for the absence of microscopic shear bands in the HPT-processed duplex stainless steels: 1) the α -phase and γ -phase are of different properties which may suppress the growth of shear bands at low strain levels; 2) microscopic shear bands may quickly diminish under the complex shear strain conditions of HPT, making it difficult to identify them in the material. Thus, the shear bands discussed in this work are macroscopic shear bands, which are readily observable under an OM in many materials processed by HPT.^[13,32,33]

When sufficient shear strains are imposed to the disk samples, both α -phase and γ -phase can be refined to nanostructures. Figure 8 shows the microstructures of the periphery regions of an HPT disk processed to five revolutions under 6 GPa pressure. The equivalent von Mises strain in the local region (within 2 mm to the disk periphery) was estimated to be in the range of 60–100. The sizes of the ferrite grains are in the ultrafine-grained regimes and the sizes of the austenite grains are mostly in the nano-crystalline regime. The γ -phase domains

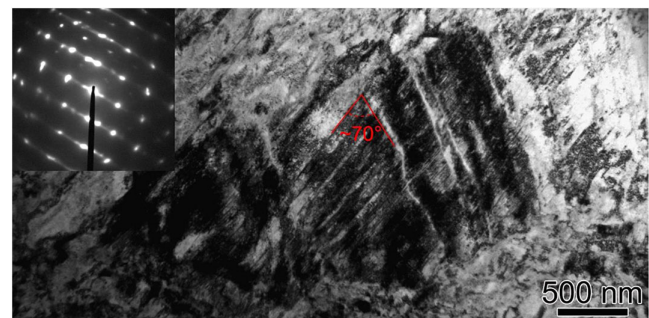


Figure 7. A TEM image showing the grain refinement process of an austenite grain containing a high density of twins. This image was taken near the center of a HPT disk processed to five revolutions under 6 GPa pressure. The inset is the diffraction pattern from the austenite grain. The angle between a white band and the $\{111\}$ twinning plane is $\approx 70^\circ$.

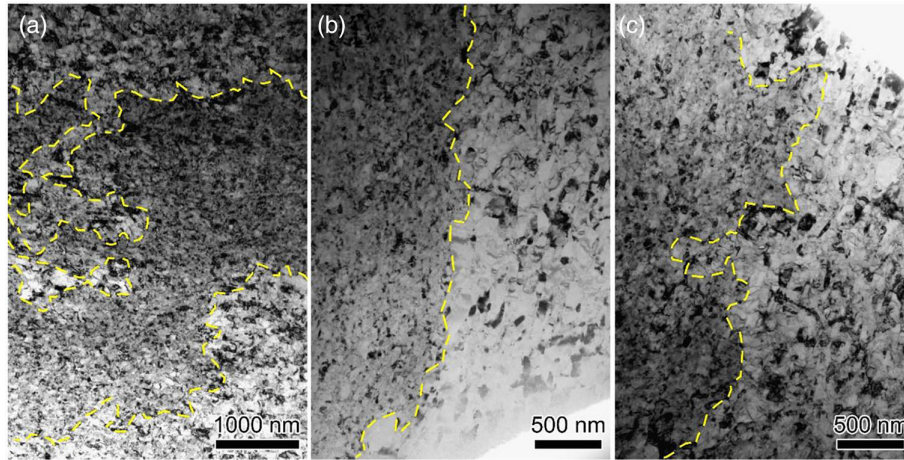


Figure 8. TEM images showing a) γ -phase domains of irregular shapes, b) a comparatively straight interface between phase domains, and c) a wavy interface between phase domains. Yellow dashed lines trace interfaces between α -phase and γ -phase domains. The images are taken from the edge of a HPT disk processed to five revolutions under 6 GPa pressure.

may possess a very complex shape as shown in Figure 8a and a small volume of ferrite grains was partially squeezed into the γ -phase domain in this particular region, thereby indicating a very complicated strain condition in the local area. As shown in Figure 8b,c, the interphase interfaces vary significantly from one area to another. The ultrafine grain sizes and active grain boundaries grant the freedom for phase domains and interphase interfaces to adapt to any shapes.

Figure 9 shows high-resolution transmission electron microscopy (TEM) images of a typical γ -grain and α -grain. Figure 9a

shows a γ -grain that contains many stacking faults. Every stacking fault has at least one end attached to the grain boundary. Figure 9b is an enlarged image of the selected area in Figure 9a. The longest extrinsic stacking fault in the grain, as shown in Figure 9a, has one end attached to the grain boundary, as shown in Figure 9b. The extrinsic stacking fault shifted the atoms on two adjacent atomic planes away from the original positions of a perfect lattice structure. Figure 9c shows an α -grain that has most of the dislocations located close to the grain boundary, as shown in Figure 9d.

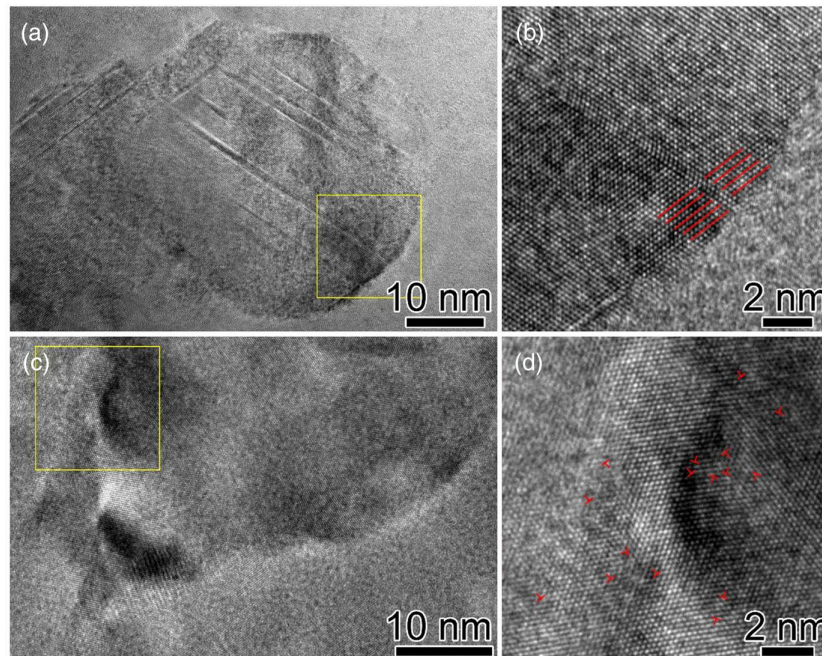


Figure 9. High-resolution TEM images showing atomic structures of grains at the edge of a HPT disk processed to five revolutions under 6 GPa pressure: a) an austenite grain viewed at $[011]$ zone axis, b) an enlarged image of the selected area in (a,c) a part of a ferrite grain at $[\bar{1}\bar{1}\bar{1}]$ zone axis, and d) an enlarged image of the selected area in (c). (Red lines trace $(\bar{1}\bar{1}\bar{1})$ planes inclined to an extrinsic stacking fault. A red “T” marks a dislocation component.)

3. Discussion

According to Equation (1), the shear strain imposed by HPT will gradually shear and twist each unit volume in the sample. If each unit volume is in the shape of a cube, the shear strain imposed by HPT causes the top surface of the cube to shear and gives a simultaneous shift with respect to the bottom surface. A detailed description of the ideal shear strain imposed by HPT is given in previous studies.^[1,34,35] However, deviations from the ideal situation are always encountered in real practice, resulting in the heterogeneity of local shear strain. Macroscopic shear strain heterogeneity in the form of shear turbulence, shear vortices, and shear bands, as shown in Figure 3 and 4, clearly reveals the complexities of local shear strain. Thus, the major outstanding issue is to determine the types of deformation mechanisms that are capable of strain accommodation.

In the case of crystalline materials, dislocation slip and/or deformation twinning are common strain accommodation mechanisms. However, both dislocation slip and deformation twinning have directionalities, which are strictly limited by the available slip systems and twinning systems, respectively. In the current case, the α -phase was deformed by the dislocation slip and γ -phase was deformed by both dislocation slip and twinning, as revealed by comparing Figure 5 and 6. As shown in Figure 6, the α -phase domain contains dislocation substructures that tend to elongate in the vertical direction. This indicates that the local shear strain was roughly in the vertical direction.^[35] In contrast, the γ -phase was deformed mainly by twinning due to the low stacking-fault energy and high imposed pressure/stress.^[27,36] The coherent twin boundaries have an acute angle to the direction of elongation of the dislocation substructures in the α -phase, indicating that local shear stress favors the twinning shear. The high densities of deformation twins and geometrically necessary dislocations at the phase boundaries are capable of accommodating the small but complex local shear strain that leads to wavy phase/grain boundaries.

There is a critical issue that if once an austenite grain is filled with a high density of deformation twins as shown in Figure 6, the grain then possesses an apparent flow stress anisotropy because dislocation slip and twinning are much easier in directions parallel to the coherent boundaries of the high-density nano-twins than in other directions.^[4,37] As shown in Figure 7, the austenite grain has been "sliced" into a few pieces by white bands. The white bands have an angle of $\approx 70^\circ$ to the coherent twin boundaries, indicating that the white bands are deformation twins of another twinning system that has lost coherency due to strain localization. This grain can be sheared in directions parallel to the white bands but hardly changes its shape in other ways. Thus, it is obvious that this austenite grain is incapable of accommodating a large strain such as a shear vortex. By contrast, as the grain sizes are reduced to the ultrafine-grained regime and lower, the γ -phase domains possess very complex shapes, as shown in Figure 8. For the duplex steel used in the current experiment, a shear strain of above 20 was necessary to achieve substantial grain refinement to the ultrafine-grained regime. Consider the fact that macroscopic shear vortices and shear bands were only observed in the HPT disks processed to three and more revolutions and in the regions where the local von Mises strains were estimated to be larger than 40. Thus, a localized large shear strain

in the form of shear vortices and shear bands can only be accommodated with the assistance of grain boundary-mediated processes that are characteristic deformation mechanisms of ultrafine grains and nano-grains.^[38] Figure 9 provides solid evidence of grain boundary-mediated plasticity in the nanocrystalline duplex stainless steel processed by HPT to five revolutions. As shown in Figure 9a,b, large numbers of stacking faults were formed in the γ -grain by the emission of partial dislocations from the grain boundary. As shown in Figure 9c,d, the majority of the dislocations in an α -grain are located close to the grain boundary, but in the interior of the grains the dislocation density is low. Thus, the plastic strain at the edge of the five-revolutions HPT sample is mainly accommodated by grain boundary-mediated deformation mechanisms.^[8,39–43] There are reports showing that at the hardening stage of HPT processing the major work is performed in causing grain refinement.^[44] Once the grain sizes reach the new steady state, a further increase in strain would be mainly accommodated by dynamic recovery,^[8] grain rotation^[39,40] and grain boundary sliding.^[41,42] These grain boundary-mediated activities are effective in redistributing and reshaping the phase domains.^[44]

The shear strain carried by shear turbulence is complex but not necessarily high, and it is strongly related to the initial shapes and orientations of the γ -phase domains. As shown in Figure 7, the irregularity of the austenite grain has sizes that are comparable to shear turbulence patterns at low strain levels which were observed near the centers of two- and three-revolutions HPT samples in earlier work.^[12,13] In addition, the stream-like shear turbulences shown in Figure 4c,d are very thin and interweaved with other shear structures such as shear bands and shear vortices. This indicates that shear turbulence in the high-strain region and in the low-strain region may be accommodated by different deformation mechanisms.

There are numerous reports showing that when the imposed shear strain is sufficiently high, the shear strain patterns throughout the disk become comparable to the ideal situation.^[10,13,34] However, as shown in Figure 3b, a ring-shaped region featuring shear instability outlined the periphery of the 16-revolution disk. This indicates that even at a very high strain level the ideal shear strain patterns may not develop because the top and bottom anvils of the HPT facility may be misaligned by approximately 100 μm or larger.^[14] In fact, the major experimental factor that causes shear strain instability including shear bands, shear vortices, and even double shear swirls^[13] is anvil misalignment.^[14]

The shear strain was transmitted by the frictional force between the anvils and the disk sample.^[1] Therefore, the possible effect of any fretting fatigue on the deformation of the sample cannot be ruled out. Very little information is available on fretting fatigue in HPT processing. However, detached debris on the surfaces and outflow chips at the periphery of the HPT disks have been observed and this may be related to fretting fatigue. Fretting fatigue has been strictly limited to the HPT sample surface and this is probably because of the significant grain refinement which is effective in suppressing the initiation of cracks and accommodating a plastic strain amplitude during fatigue.^[45] The microstructures observed in this work were revealed on the polished surface where the effect of fretting fatigue has been purposely eliminated. The effect of fretting fatigue on the

deformation of HPT samples is of importance in the engineering practice of HPT^[46] and will be investigated in future work.

4. Conclusions

Macroscopic heterogeneity induced by HPT was revealed by the complex shear strain patterns including shear bands, shear vortices, and shear turbulences. While shear turbulence was observed in nearly all strain levels, shear bands and shear vortices were found only at high strain levels where grain refinement had already reached the steady state.

Microscopic local shear strain heterogeneities were revealed by shapes of the grains and phase domains and the traces of the grain boundaries and phase boundaries. At low strain levels, when the grain sizes are in the scale of micrometers, dislocation slip and deformation twinning accommodate local shear strain. Thus, the shapes of the grains and phase domains are determined by the active slip systems and twinning systems. The freedoms for changing the shapes of grains and phase domains are then very limited. Therefore, complex shear patterns such as macroscopic shear bands and shear vortices cannot form at these low strain levels.

In the current work, it is proven that the intrinsic factor required for the formation of complex shear patterns is well-developed ultrafine grains and/or nano-grains. Once the grains are refined to the ultrafine-grained regime and the nano-crystalline regime, further shear straining is mainly accommodated by grain boundary-mediated mechanisms including grain rotation and grain boundary sliding. These grain boundary-mediated activities are effective in redistributing and reshaping the phase domains, thus allowing the formation of macroscopic shear bands and shear vortices.

5. Experimental Section

A commercial DP3W duplex stainless steel containing approximately equal volume fractions of the body-centered cubic ferrite (α) phase and face-centered cubic austenite (γ) phase was used in this investigation. For additional details of the DP3W duplex stainless steel, readers are referred to relevant literatures.^[13,28,47] Disks with a diameter of ≈ 9.8 mm and a thickness of ≈ 1.7 mm were cut from the steel plates. Both sides of each disk were polished using abrasive papers (from 180 to ≈ 4000 grit) to make a series of disk samples having final thicknesses of 0.79–0.80 mm ready for HPT processing. The HPT experiments were conducted under quasi-constrained conditions with a rotational speed of 1 rpm. A total of 14 disks were processed under 6 GPa pressure for 1, 2, 3, 5, 6, 10, and 16 revolutions, and 2 disks were processed under 8 GPa pressure for 16 revolutions. Based on our experimental observations and available literature,^[48,49] slippage in HPT processing was minimized with an applied pressure above 3 GPa. There was no recorded slippage for samples processed less than five revolutions in these experiments. The reason for using the quasi-constrained HPT method is that it overcomes the drawbacks of sample thinning and increased torque when processing, using unconstrained and fully constrained HPT methods, respectively.^[50]

OM and TEM analysis were conducted on the as-received and HPT samples to help in revealing the nature of the heterogeneity of the local shear strain imposed by HPT. To achieve good contrast between the α -phase and γ -phase under OM, several different methods were evaluated for preparing the material surface. It was eventually found that there are two methods that lead to promising results: 1) By using a Struers

OP-U-0.04 μm suspension in the final polishing stage, consistent but light contrast between the two phases was revealed throughout the entire polished surface. 2) Chemical etching by a solution of 45% water, 30% nitric acid, 10% hydrofluoric acid, and 15% hydrochloric acid significantly improved the contrast between the two phases, but the results were inconsistent and they were affected by the etching time, temperature, and humidity. Extensive OM analysis was conducted with an Olympus BX-61 OM and a ZEISS-Axio-Vert-A1 OM. Each TEM sample was taken parallel to the disk surface, and prepared by electropolishing using a Struers TenuPol-5 jet electropolishing unit and a solution of 23% perchloric acid and 77% acetic acid, under an operating voltage of 20 V and at a temperature of 20 °C, until a central perforation surrounded by a thin area was formed. Careful control of the electropolishing condition can guarantee a nearly 100% success rate and excellent sample quality. TEM characterization was performed with a Philips CM12 microscope operating at 120 kV and a Tecnai G2 20 microscope operating at 200 kV.

Acknowledgements

This work was supported by the National Natural Science Foundation of China (51601094 (Y.C.)), and the Fundamental Research Funds for the Central Universities (30918011342 (H.Z.) and 30919011412 (Y.Z.)). This work was also supported in part by the National Science Foundation of the United States (DMR-1810343 (M.K.)) and the European Research Council (ERC Grant 267464-SPDMETALS (T.G.L.)). The authors are thankful for the technical support from the Jiangsu Key Laboratory of Advanced Micro & Nano Materials and Technology and the Materials Characterization Facility of Nanjing University of Science and Technology.

Conflict of Interest

The authors declare no conflict of interest.

Keywords

deformation twinning, high-pressure torsion, microstructures, shear strains, steels

Received: April 30, 2019

Revised: August 18, 2019

Published online:

- [1] A. P. Zhilyaev, T. G. Langdon, *Prog. Mater. Sci.* **2008**, *53*, 893.
- [2] T. G. Langdon, *Acta Mater.* **2013**, *61*, 7035.
- [3] R. Z. Valiev, Y. Estrin, Z. Horita, T. G. Langdon, M. J. Zehetbauer, Y. T. Zhu, *Mater. Res. Lett.* **2016**, *4*, 1.
- [4] Y. Cao, S. Ni, X. Z. Liao, M. Song, Y. T. Zhu, *Mater. Sci. Eng. R* **2018**, *133*, 1.
- [5] K. S. Kormout, R. Pippan, A. Bachmaier, *Adv. Eng. Mater.* **2017**, *19*, 1600675.
- [6] R. B. Figueiredo, P. H. R. Pereira, M. T. P. Aguilar, P. R. Cetlin, T. G. Langdon, *Acta Mater.* **2012**, *60*, 3190.
- [7] A. P. Zhilyaev, G. V. Nurislamova, B. K. Kim, M. D. Baró, J. A. Szpunar, T. G. Langdon, *Acta Mater.* **2003**, *51*, 753.
- [8] C. Xu, Z. Horita, T. G. Langdon, *Acta Mater.* **2008**, *56*, 5168.
- [9] M. Kawasaki, B. Ahn, T. G. Langdon, *Acta Mater.* **2010**, *58*, 919.
- [10] Y. Cao, M. Kawasaki, Y. B. Wang, S. N. Alhajerji, X. Z. Liao, W. L. Zheng, S. P. Ringer, Y. T. Zhu, T. G. Langdon, *J. Mater. Sci.* **2010**, *45*, 4545.
- [11] C. Xu, Z. Horita, T. G. Langdon, *Acta Mater.* **2007**, *55*, 203.

- [12] Y. Cao, Y. B. Wang, S. N. Alhajeri, X. Z. Liao, W. L. Zheng, S. P. Ringer, T. G. Langdon, Y. T. Zhu, *J. Mater. Sci.* **2010**, *45*, 765.
- [13] Y. Cao, Y. B. Wang, R. B. Figueiredo, L. Chang, X. Z. Liao, M. Kawasaki, W. L. Zheng, S. P. Ringer, T. G. Langdon, Y. T. Zhu, *Acta Mater.* **2011**, *59*, 3903.
- [14] Y. Huang, M. Kawasaki, T. G. Langdon, *Adv. Eng. Mater.* **2013**, *15*, 747.
- [15] Y. Z. Tian, S. D. Wu, Z. F. Zhang, R. B. Figueiredo, N. Gao, T. G. Langdon, *Acta Mater.* **2011**, *59*, 2783.
- [16] J.-K. Han, D. K. Han, G. Y. Liang, J.-I. I. Jang, T. G. Langdon, M. Kawasaki, *Adv. Eng. Mater.* **2018**, *20*, 1800642.
- [17] A. P. Zhilyaev, F. Gálvez, A. Sharafutdinov, M. T. Pérez-Prado, *Mater. Sci. Eng. A* **2010**, *527*, 3918.
- [18] Y. B. Wang, Y. H. Zhao, Q. Lian, X. Z. Liao, R. Z. Valiev, S. P. Ringer, Y. T. Zhu, E. J. Lavernia, *Scr. Mater.* **2010**, *63*, 613.
- [19] Y. B. Wang, M. Louie, Y. Cao, X. Z. Liao, H. J. Li, S. P. Ringer, Y. T. Zhu, *Scr. Mater.* **2010**, *62*, 214.
- [20] Y. T. Zhu, X. L. Wu, *Mater. Res. Lett.* **2019**, *7*, 393.
- [21] X. H. An, S. M. Zhu, Y. Cao, M. Kawasaki, X. Z. Liao, S. P. Ringer, J. F. Nie, T. G. Langdon, Y. T. Zhu, *Appl. Phys. Lett.* **2015**, *107*, 011901.
- [22] F. J. Humphreys, M. Hatherly, *Recrystallization and Related Annealing Phenomena*, 2nd ed., (Eds: F. J. Humphreys, M. Hatherly), Elsevier, Oxford **2004**, p. 11.
- [23] S. D. Antolovich, R. W. Armstrong, *Prog. Mater. Sci.* **2014**, *59*, 1.
- [24] X. L. Ma, H. Zhou, J. Narayan, Y. T. Zhu, *Scr. Mater.* **2015**, *109*, 89.
- [25] J. Gu, L. X. Zhang, S. Ni, M. Song, *Scr. Mater.* **2016**, *125*, 49.
- [26] L. Liu, J. Wang, S. K. Gong, S. X. Mao, *Phys. Rev. Lett.* **2011**, *106*, 175504.
- [27] Y. Cao, Y. B. Wang, X. Z. Liao, M. Kawasaki, S. P. Ringer, T. G. Langdon, Y. T. Zhu, *Appl. Phys. Lett.* **2012**, *101*, 231903.
- [28] Y. Cao, Y. B. Wang, X. H. An, X. Z. Liao, M. Kawasaki, S. P. Ringer, T. G. Langdon, Y. T. Zhu, *Acta Mater.* **2014**, *63*, 16.
- [29] H. Paul, A. Morawiec, J. H. Driver, E. Bouzy, *Int. J. Plast.* **2009**, *25*, 1588.
- [30] X. H. An, S. D. Wu, Z. G. Wang, Z. F. Zhang, *Prog. Mater. Sci.* **2019**, *101*, 1.
- [31] X. H. An, Q. Y. Lin, S. D. Wu, Z. F. Zhang, R. B. Figueiredo, N. Gao, T. G. Langdon, *Philos. Mag.* **2011**, *91*, 3307.
- [32] Y. Z. Tian, X. H. An, S. D. Wu, Z. F. Zhang, R. B. Figueiredo, N. Gao, T. G. Langdon, *Scr. Mater.* **2010**, *63*, 65.
- [33] Y. Huang, M. Kawasaki, T. G. Langdon, *Adv. Eng. Mater.* **2013**, *15*, 747.
- [34] M. Hafok, R. Pippan, *Scr. Mater.* **2007**, *56*, 757.
- [35] M. Hafok, R. Pippan, *Philos. Mag.* **2008**, *88*, 1857.
- [36] Y. Cao, Y. B. Wang, X. H. An, X. Z. Liao, M. Kawasaki, S. P. Ringer, T. G. Langdon, Y. T. Zhu, *Scr. Mater.* **2015**, *100*, 98.
- [37] L. Lu, X. Chen, X. Huang, K. Lu, *Science* **2009**, *323*, 607.
- [38] Z. W. Shan, E. A. Stach, J. M. K. Wiezorek, J. A. Knapp, D. M. Follstaedt, S. X. Mao, *Science* **2004**, *305*, 654.
- [39] L. H. Wang, J. Teng, P. Liu, A. Hirata, E. Ma, Z. Zhang, M. W. Chen, X. D. Han, *Nat. Commun.* **2014**, *5*, 4402.
- [40] Y. B. Wang, B. Q. Li, M. L. Sui, S. X. Mao, *Appl. Phys. Lett.* **2008**, *92*, 011903.
- [41] M. Y. Gutkin, I. A. Ovid'ko, N. V. Skiba, *Acta Mater.* **2003**, *51*, 4059.
- [42] X. Y. Li, Y. J. Wei, W. Yang, H. J. Gao, *Proc. Natl. Acad. Sci.* **2009**, *106*, 16108.
- [43] L. H. Wang, X. D. Han, P. Liu, Y. H. Yue, Z. Zhang, E. Ma, *Phys. Rev. Lett.* **2010**, *105*, 135501.
- [44] Y. F. Liu, F. Wang, Y. Cao, J. F. Nie, H. Zhou, H. B. Yang, X. F. Liu, X. H. An, X. Z. Liao, Y. H. Zhao, Y. T. Zhu, *Scr. Mater.* **2019**, *162*, 316.
- [45] H. W. Huang, Z. B. Wang, J. Lu, K. Lu, *Acta Mater.* **2015**, *87*, 150.
- [46] R. K. Reeves, D. W. Hoepfner, *Wear* **1976**, *40*, 395.
- [47] S. K. Samudrala, P. J. Felfer, V. J. Araullo-Peters, Y. Cao, X. Z. Liao, J. M. Cairney, *Ultramicroscopy* **2013**, *132*, 158.
- [48] K. Edalati, Z. Horita, T. G. Langdon, *Scr. Mater.* **2009**, *60*, 9.
- [49] M. Kamrani, V. I. Levitas, B. Feng, *Mater. Sci. Eng. A* **2017**, *705*, 219.
- [50] R. B. Figueiredo, P. R. Cetlin, T. G. Langdon, *Mater. Sci. Eng. A* **2012**, *528*, 8198.